Nanoscale

PAPER

View Article Online
View Journal | View Issue

Cite this: *Nanoscale*, 2025, **17**, 904

Biodegradable cellulose nanocrystal composites doped with carbon dots for packaging and anticounterfeiting applications†

Shiva Singh, [a] Keshav Dev,[b] Shakshi Bhardwaj,[a] Dakuri Ramakanth, [a] Khushboo Rani Singh,[c] Krishna Mohan Poluri, [c] Kaushik Ghosh [b] and Pradip K. Maji *[a]

Developing sustainable and multifunctional materials is imperative for advancing anti-counterfeiting measures, sensing technologies, and intelligent packaging solutions. Concurrently, materials based on carbon dots (CDs) and cellulose nanocrystals (CNCs) are becoming established in such applications. Therefore, herein, we present the fabrication and characterization of water-based CDs and CNCs from *Vigna mungo* (black lentil: BL). The carbon dots (CD_{BL}) were doped with nitrogen (NCD_{BL}) and sulfur (SCD_{BL}). These CDs were then utilized as anti-counterfeit inks and multifunctional sensor films when loaded in a biodegradable CNC_{BL} matrix. These CD_{BL}, SCD_{BL}, and NCD_{BL} exhibited diameters of 3.7, 5.3, and 5.5 nm, respectively, with bandgap values ranging from 3.65 eV to 2.95 eV. For anti-counterfeiting, CDs/CNC_{BL}-based inks were applied to white sheets, rendering them invisible under normal lighting conditions and visible under UV light (365 nm). NCD_{BL} exhibited sensitivity towards pH changes (2–12), demonstrating the sensing potential of NCD_{BL}/CNC_{BL} films for monitoring food freshness. Additionally, NCD_{BL}/CNC_{BL}-based films have exhibited effective control over microbial load due to nitrogen doping. These films biodegrade within 29 days when buried in soil after use. This innovative approach presents multifunctional films that address critical needs in sensing, anti-counterfeiting, and intelligent packaging and opens new avenues for creating eco-friendly, multifunctional materials.

Received 13th September 2024,
Accepted 13th November 2024

DOI: 10.1039/d4nr03768e

rsc.li/nanoscale

1. Introduction

Counterfeiting and food security are significant worldwide issues resulting in industrial losses of up to trillions of dollars, and these costs are growing yearly. Moreover, the act of producing counterfeit items such as drugs, fabricated food packages, certifications, and electronics poses a direct threat to human health, social fairness, and national security.[1] Effective techniques for combating counterfeiting include anti-counterfeiting labels, inks, tamper-proof features, and optical security devices that are easily verifiable and readily available, such as luminous holograms, magnetic inks, and microprinting.[2] Recently, reversible responsiveness has been proposed as a means to enhance the security of optical anti-counterfeiting labels.[3] This is achieved by including various operation modes.[3] Repeated mode switching might lead to the formation of degradation side-products. In addition, once the fluorescent molecule is made known, the majority of these methods, although expensive and complex, can be replicated over a span of 18 months.[4]

Several fluorescent materials, such as semiconductor quantum dots, organic dyes, and carbon dots (CDs), have been extensively studied for this specific use.[5,6] CDs are notable among these materials due to their exceptional stability, nominal toxicity, abundant precursors, and environmentally favorable manufacturing methods.[7] CDs have been proposed as triple mode emission carbon dots for anti-counterfeiting by Jiang *et al.* They have propped CDs as a nearly colorless ink for anti-counterfeit purposes with three types of detection modes.[8] Luo *et al.* established a literature review for using CDs as nanosensors for food quality and safety assessment.[9] Ananthi *et al.* have proposed fully biodegradable CD composites for active food packaging applications.[10] Similarly, Althawab *et al.* have proposed CD-based composites with anti-

[a]*Department of Polymer and Process Engineering, Indian Institute of Technology Roorkee, Saharanpur Campus, Saharanpur-247001, India.*
E-mail: pradip@pe.iitr.ac.in; Tel: +91-7895965010
[b]*Department of Chemistry, Indian Institute of Technology, Roorkee 247667, India*
[c]*Department of Biosciences and Bioengineering, Indian Institute of Technology Roorkee, Roorkee-247667, Uttarakhand, India*

† Electronic supplementary information (ESI) available. See DOI: https://doi.org/10.1039/d4nr03768e

bacterial properties for food packaging and security.[11] Some literature studies also reported the integration of CDs into cellulose matrices for targeted applications like bioimaging, sensing, photocatalysis, and light screening.[12–19] Specifically, cellulose nanocrystals (CNCs) have been explored with CDs for various applications due to their self-assembly behavior and surface functionalities.[20,21]

CDs have been utilized separately for anticounterfeiting[8,22–24] and food packaging applications;[25–27] however, studies evaluating CDs with combined properties, such as anticounterfeiting, sensing, antimicrobial activity, and biodegradability, which are essential for multifunctional applications, have been limited. In the context of food packaging, there is a critical need for new material composites that integrate these functionalities to provide effective and practical real-time solutions. CDs have been synthesized from bio-based materials such as honey, sugarcane bagasse, grape seeds, and orange peels. However, these materials often result in low quantum yields due to their relatively low carbon content; honey contains 23.5%,[28] sugarcane bagasse 24.7%,[29] and grape seeds 14.0%[30] carbon. Since higher carbon content typically leads to better CD yields, exploring bio-sources rich in carbon is essential to achieve more efficient synthesis.

In response to these limitations, we have utilized waste derived from *Vigna mungo* (black lentil: BL) to produce carbon dots (CD_{BL}) and cellulose nanocrystals (CNC_{BL}) for the first time, targeting applications in anti-counterfeiting, food security, and freshness monitoring. BL contains approximately 41.63% carbon, motivating our choice of it as a superior precursor for CD synthesis compared to previously used sources. The CD_{BL} was derived from discarded black lentils and these can be doped with sulfur and nitrogen. These CD_{BL} particles were then incorporated into a CNC_{BL} matrix, creating a material that serves as a multimodal ink, remaining invisible under normal light but visible under UV light (365 nm). Additionally, this material was formed into films that function as fluorescent sensors for food preservation. These films demonstrated a strong ability to eradicate microorganisms and inhibit bacterial growth while being biodegradable in soil within 29 days. Combining these unique properties makes our material a pioneering option in the food packaging industry, offering enhanced safety, quality, and environmental responsibility. This innovative material uniquely integrates anti-counterfeiting, food security, antibacterial activity, and biodegradability, presenting a novel, comprehensive solution for various practical applications.

2. Results and discussion

2.1. Proximate analysis

As we report the first-time extraction of CNC_{BL} and CDs (CD_{BL}, SCD_{BL}, and NCD_{BL}) from BL shell waste, it becomes vital to also report the constituents of BL shell waste. Proximate analysis was performed to determine the proportions of ash (1.60 ± 0.04), solvent extractive components (8.21 ± 0.85), alpha-cellulose, holocellulose (38.40 ± 1.42), moisture (1.71 ± 0.07), and acid-insoluble lignin (Klason) (18.80 ± 1.09) in *Vigna mungo* shell waste (three independent sets of experiments were performed for each analysis). The methods were performed in triplicate, and the standard deviation of the values was computed. The computed values are condensed in Table S1.† Furthermore, the conversion rate from CPC_{BL} to CNC_{BL} was determined to be 87%. Ultimate analysis was conducted to measure the elemental composition of several samples, including Raw_{BL}, CPC_{BL}, and CNC_{BL}. An incremental decline in the levels of nitrogen and carbon was seen in the raw CPC_{BL} due to the elimination of carbon- and nitrogen-containing lignin and wax. In addition, during the conversion from CPC_{BL} to CNC_{BL}, a little carbon content loss was found due to the decrease in carbon atoms in the amorphous areas. Ultimate analysis and elemental analysis are summarised in Tables S1 and S2,† respectively. The comprehensive significance and elemental analysis methods are reported in section S1.†

2.2. Structural and morphological analysis of CNC_{BL}

Scheme 1 represents the preparation of CDs, their doping with sulfur (SCD_{BL}) and nitrogen (NCD_{BL}), and film formation with CNC_{BL} of prepared CDs. For structural assessment, the samples from every chemical treatment of BL were analyzed using FTIR. A significant decrease in transmittance occurs between 3800 and 3000 cm^{-1}, indicating –OH stretching and hydrogen bonding. The 2900–2700 cm^{-1} peaks indicate C–H_n (n = 1,2) stretching; the peak turned from shouldered to single due to chemical treatments producing only CH_2 carbons in the case of raw to CPC_{BL} samples. Raw to CNC_{BL} samples have characteristic peaks at 1260, 1370, 1160, 1050, 900, and 1100–1030 cm^{-1}, indicating native cellulose.[31–33] These peaks indicate C–OH stretching, C–H bending, C–O–C glycosidic ether linkage, C–O–C pyranose ring, C–H deformation (H–C–O–C beta-linkage), and C–O stretching and rocking vibration, as depicted in Fig. S1(a).† Acid hydrolysis destroyed the amorphous portion of cellulose, resulting in crystalline cellulose and enhanced particle XRD crystallinity at 15.48°, 22.5°, and 35.5° corresponding to (110), (200), and (004) planes. The crystallinity index (C.I.) using powder XRD verifies amorphous removal and crystalline domain preservation.[20,34] Segal method C.I. values for Raw_{BL}, CPC_{BL}, and CNC_{BL} samples are 40.4%, 82.3%, and 88.9%, as shown in Fig. S1(b).†[35] Eliminating amorphous components like hemicellulose and lignin improves Raw_{BL} to CPC_{BL} C.I. values. Acid hydrolysis removes amorphous cellulose and increases CNC_{BL} crystallinity, increasing the C.I. The XPS spectra in Fig. 1(a) show electrons from carbon and oxygen 1s orbitals with two notable peaks at 282 and 530 eV. In Fig. S1(c),† CNC_{BL} carbon bond connections cause three unique peaks in the high-resolution deconvoluted C 1s spectra. The C sp^3 exhibits four peaks around 284.01 eV, 285.4 eV, 288.0 eV, and 288.9 eV. These peaks are associated with sp^2 C═C, C–C/H, C–S/N/O (pyranose ring), and C═O species, respectively. The O bond (primary and secondary alcohols) at 286.7 eV, and the O–C–O link (pyranose ring, glycosidic connection) at 288.8 eV.[36,37] The deconvoluted O 1s spectra has two peaks, as shown in Fig. S1(d).†

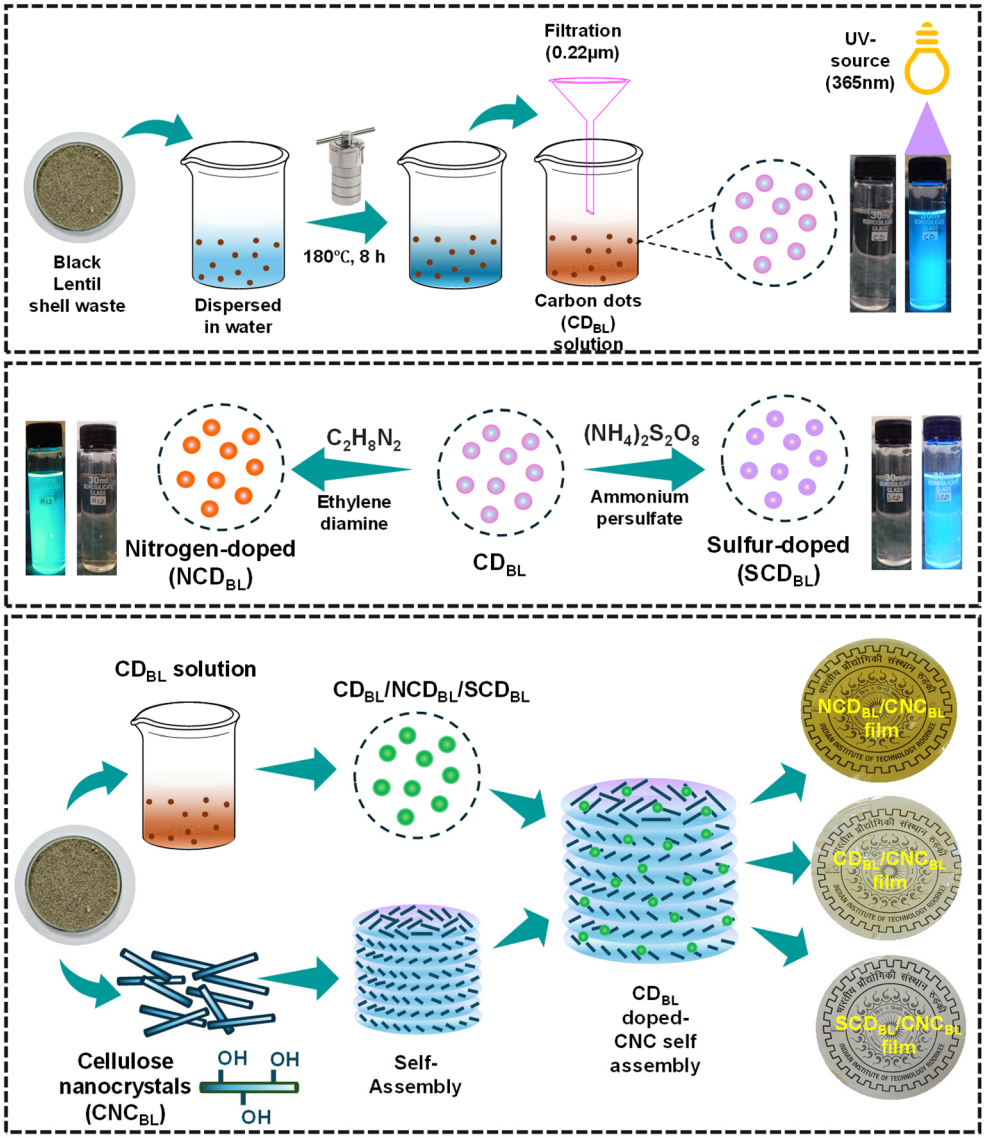

Scheme 1 Graphical representation of the preparation of CDs, their doping with sulfur (SCD_{BL}) and nitrogen (NCD_{BL}), and film formation with CNC_{BL} of the prepared CDs.

The first peak of the pyranose ring has one bonded O from C–O–H and C–O–C at 532.9 eV and a second with water and carboxylic acid functional groups at 534.5 eV.[38] Table S2† summarises the bond area under the curve values by deconvolution. FESEM assessed morphological changes from Raw_{BL} to CNC_{BL}, as shown in Fig. S2.† Fibers grow stiffer without lignin, waxes, and hemicellulose. These binding substances were removed, and holes are evident in the Raw_{BL} to CPC_{BL} samples, as shown in Fig. S2(a) and (b).† Acid hydrolysis eliminates the amorphous phase of cellulose fibers, resulting in a 20 nm rod (Fig. S2(c)).† This section confirms the successful extraction of CNC_{BL}. The upcoming section focuses on CD_{BL} preparation from the BL waste and the doping of CDs using nitrogen and sulfur from the Raw_{BL} waste material. This will also deal with the CD_{BL} structural arrangements and morphological analysis.

2.3. Structural and morphological analysis of CD_{BL}, SCD_{BL}, and NCD_{BL}

An XPS examination was performed to assess the elemental composition and chemical bonding of the prepared CD_{BL}, SCD_{BL}, and NCD_{BL}. The main constituents identified in the produced CDs were carbon (C) and oxygen (O), together with small quantities of silicon (Si), calcium (Ca), and magnesium (Mg), which align with the makeup of the source material shown in Table S2.†[39] In addition, the study showed that the doped SCD_{BL} and NCD_{BL} had sulfur and nitrogen loadings of 1.2% and 2.4%, respectively, but below one percentage of sulfur and nitrogen were found in the CD_{BL} sample.

The structure of the prepared CDs has been affirmed using XPS and FTIR. Fig. 1(a) shows the XPS analysis results, which

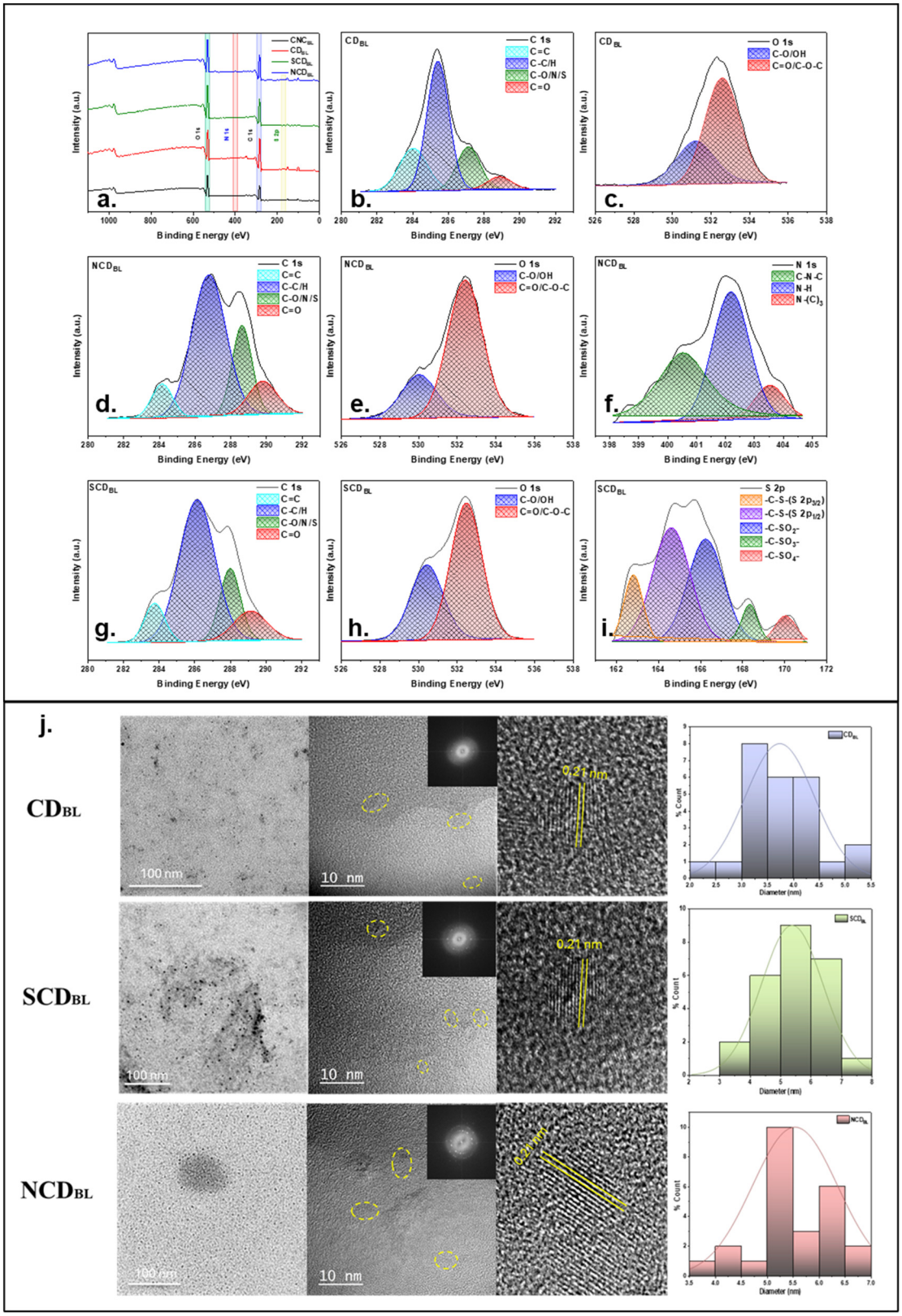

Fig. 1 XPS analysis of (a) CNC_{BL}, CD_{BL}, SCD_{BL}, and NCD_{BL}; (b) C 1s spectra of CD_{BL}; (c) O 1s spectra of CD_{BL}; (d) C 1s spectra of NCD_{BL}; (e) O 1s spectra of NCD_{BL}; (f) N 1s spectra of NCD_{BL}; (g) C 1s spectra of SCD_{BL}; (h) O 1s spectra of SCD_{BL}; (i) S 2p spectra of SCD_{BL} and (j) HR-TEM analysis with lattice fringe analysis (fast Fourier transform pattern inset) and particle size distribution of CD_{BL}, SCD_{BL}, and NCD_{BL}.

indicate the presence of four unique peaks at binding energies of 532.0 eV, 399.9 eV, 284.8 eV, and 168.3 eV.[40] These peaks correspond to the elements O 1s, N 1s, C 1s, and S 2p, respectively. These peaks were deconvoluted using a Gaussian fit with 500 iterations, and the plots were fitted under one chi-square value (Table S2†). The N 1s peak is absent in the CD_{BL} and SCD_{BL} samples, whereas the S 2p peak is not detected in the CD_{BL} and NCD_{BL} samples. The deconvoluted C 1s spectrum with high resolution (Fig. 1(b), (d) and (g) for CD_{BL}, NCD_{BL}, and SCD_{BL}, respectively) exhibits four peaks around 284.01 eV, 285.4 eV, 288.0 eV, and 288.9 eV. These peaks are associated with sp^2 C═C, C–C/H, C–S/N/O (epoxy and alkoxy), and C═O species, respectively.[41,42] For both SCD_{BL} and NCD_{BL}, the peak intensity at 286.0 eV is enhanced due to sulfur and nitrogen doping, respectively. This confirms the establishment of chemical bonds between the CDs and the dopants.

The deconvoluted O 1s spectra of CD_{BL}, SCD_{BL}, and NCD_{BL} (Fig. 1(c), (e) and (h) for CD_{BL}, NCD_{BL}, and SCD_{BL}, respectively) exhibit two distinct oxygen binding energies at 531.89 eV and 533.02 eV, representing C–O/OH and C═O/C–O–C bonds, respectively. The ratio of C═O/C–O–C-type bonds is higher in the doped samples compared to that in the CD_{BL}.[43,44] A high-resolution spectrum was acquired for N 1s of NCD_{BL} and S 2p of SCD_{BL} to acquire insight into the establishment of bonds. The deconvoluted N 1s spectrum of NCD_{BL} (Fig. 1(f)) reveals three prominent peaks at 400.42 eV, 402.12 eV, and 403.52 eV, signifying the existence of C–N–C, N–(C)3, and N–H bonds, respectively.[44] The S 2p spectrum of SCD_{BL} (Fig. 1(i)) exhibits three distinct peaks at energy levels of 164.0 eV, 166.0 eV, and 168.2 eV. The initial two peaks are ascribed to the $2p_{3/2}$ and $2p_{1/2}$ orbitals of the –C–S– covalent bond, whereas the final peak can be separated into constituents at 167.8 eV, 168.1 eV, and 169.3 eV, which correspond to the –C–SOx– (x = 2, 3, 4) species.[43] The quantitative assessment of these bonds is condensed in Table S2.†

The FTIR spectra of prepared CD_{BL}, SCD_{BL}, and NCD_{BL}, as depicted in Fig. S3(a),† shows that O–H and N–H bonds were responsible for the wide band at 3700–2900 cm^{-1}. The C═C/O/N broad stretching vibration peak at 1783–1485 cm^{-1} was identified.[40] Additionally, the peak at 1100 cm^{-1} indicates C–O, C–N, and C–S bonds, whereas the peak at 1051 cm^{-1} indicates $-SO^{3-}$, C–O–C, and C–O bonds.[45] The bonds observed in the FTIR analysis support the XPS analysis of the prepared CDs well.

The XRD pattern of the synthesized CDs is shown in Fig. S3(b).† The CDs show a single broad peak at 23.9°, corresponding to the (002) plane, characteristic of a graphitic structure, underscoring a complete transformation in the crystalline structure during the synthesis of CDs.[46] However, the XRD peaks of Raw_{BL} observed at 15.48°, 22.5°, and 35.5° correspond to the (110), (200), and (004) planes, which are associated with the cellulose I structure found in lignocellulosic materials, as discussed in Section 2.2.[47–49] These peaks were absent in the CDs, suggesting that the crystalline structure of the raw material has undergone significant changes during the synthesis, and the original structure is no longer present in the CDs. Such similar observations were also made by many research groups in the literature, including Pal *et al.*, Siddique *et al.*, and Mintz *et al.*[50–52]

After the structural confirmation, the morphology of CDs plays an essential role in governing the properties. Transmission electron microscopy (TEM) shows that nitrogen and sulfur doping in lignocellulosic waste-based carbon dots considerably impacts their size. Doped CDs are more uniform than undoped ones (as shown in Fig. 1(j)). Nitrogen and sulfur atoms can provide more nucleation sites during synthesis, resulting in well-dispersed dots with an increase in size due to doping diameters (3.74 ± 0.70, 5.38 ± 0.93, and 5.55 ± 0.82 nm) for CD_{BL}, SCD_{BL}, and NCD_{BL}, respectively, taking 25 dots into consideration for these calculations. These heteroatoms can also affect carbonization, changing carbon dot development dynamics and resulting in a more uniform particle size distribution (Fig. 1(j)).[40] Sulfur doping can introduce sulfur-containing functional groups, which change the surface chemistry and stability of the nanoparticles, resulting in homogeneity in size (as shown in Fig. 1(j)).[43] These alterations boost the quantum confinement effect, giving doped carbon dots unique optical and electrical capabilities, which are discussed in detail in a later section on bandgap energies. The high-resolution transmission electron microscopy (HR-TEM) images comprehensively depict the crystalline architecture of the CDs. The images demonstrate a highly crystalline structure, as indicated by the consistently clear lattice fringes across the samples. The observed interplanar spacing of 0.21 nm matches the (100) plane of graphite, suggesting that the prepared CDs have a crystalline structure similar to that of graphite.[43,53] Though it was expected that the doping of the heteroatoms might create distortions in the crystalline structures, we were not able to observe such changes in the crystalline structure, which may be due to the very low amount of doping of N (2.4%) and S (1.2%) as confirmed from XPS. The significant level of crystallinity indicates that the CDs possess a highly organized atomic structure, which is crucial for their electrical and optical characteristics. The existence of these distinct lattice fringes provides additional evidence of the high quality and consistency of the synthesized CDs, which increased with the doping of S and N and may result from the nucleation of heteroatoms as observed by FFT patterns.

2.4. Optical performance of prepared CD_{BL}

The prepared solution of CDs (CD_{BL}, NCD_{BL}, and SCD_{BL}) was evaluated for absorbance studies. We diluted the concentration of carbon dots for UV-visible and fluorescence studies. All the carbon dots are prepared in water, so we take water as a solvent. The UV spectra of the prepared CDs are depicted in Fig. 2(a); for CD_{BL}, the peaks were found near 280 nm and 320 nm, which were assigned to $\pi \rightarrow \pi^*$ and $n \rightarrow \pi^*$, respectively.[53] It is commonly recognized that the absorption peak below 300 nm represents a part of the aromatic domain $\pi \rightarrow \pi^*$ transition.[44] In SCD_{BL}, we clearly found a sharp peak at 285 nm that is for $\pi \rightarrow \pi^*$ and another peak at 325 nm for the $n \rightarrow \pi^*$ transition.[43] For NCD_{BL}, the absorption peak is around

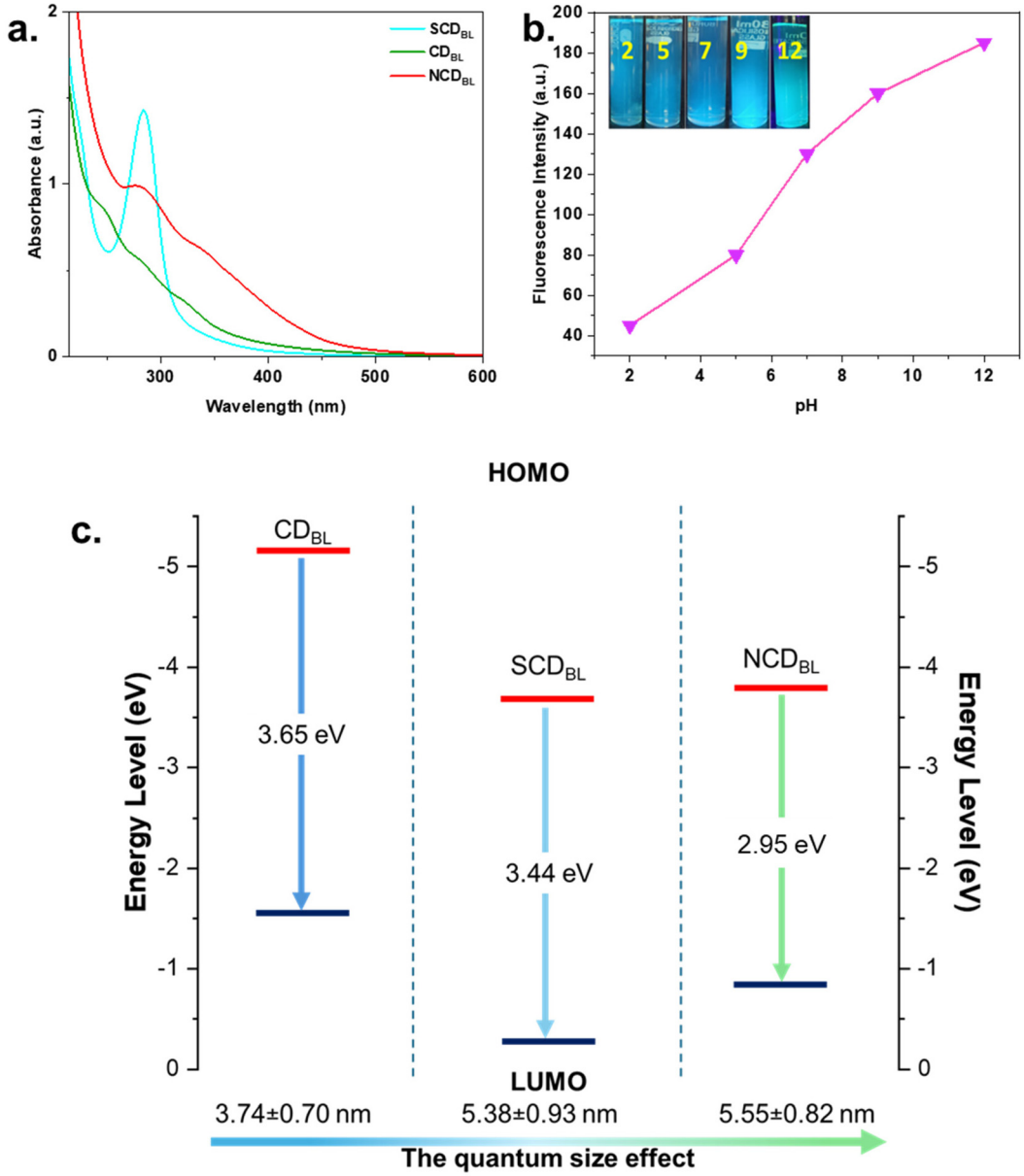

Fig. 2 (a) UV-visible spectra of the CD_{BL}, SCD_{BL}, and NCD_{BL}; (b) pH responses of the prepared NCD_{BL} with respect to its emission properties; and (c) HOMO and LUMO calculations of the CD_{BL}, SCD_{BL}, and NCD_{BL}.

275 nm, which denotes $\pi \rightarrow \pi^*$, and 340 nm, which denotes $n \rightarrow \pi^*$.[40,54] For further studies, the carbon dots were evaluated for emission characteristics.

The fluorescence emission of prepared carbon dots was evaluated at different excitation wavelengths (320–450nm), as shown in Fig. S4,† and we checked which excitation showed the highest fluorescence emission. For CD_{BL}, the excitation wavelength is 360 nm, and the highest fluorescence emission wavelength is at 455 nm. SCD_{BL} shows maximum fluorescence intensity at 415 nm with an excitation wavelength of 360 nm. For NCD_{BL} (Fig. S4†), the excitation wavelength was at 420 nm, showing maximum fluorescence intensity at 520 nm. The relative PL quantum yield (QY) of the prepared samples gradually increased from CD_{BL} to NCD_{BL}, as summarized and tabulated in Table 1. The QY of biomass-based CDs is often slightly lower than that of CDs synthesized from pure substances because it is challenging to control the composition of compounds in biomass materials precisely. Typically, reported QYs for biomass-based CDs range between 7 and 25%. However, in our study, the higher QY achieved can be attributed to the increased carbon content in our source material, black lentils (BL), which led to enhanced QY performance. Furthermore, we observed an increment in QY doped *via* nitrogen and sulfur, resulting from the enhanced nucleation caused by doping the heteroatoms.[55,56]

Furthermore, the fluorescence intensity of NCD_{BL} was also investigated over a wide pH range of pH 2–12, as shown in

Table 1 Fluorescence scan conditions, QY, and bandgap data for the as-prepared CDs

Samples	Excitation (nm)	Emission (nm)	PL range (nm)	Quantum yields (%)
CD_{BL}	360	455	360–610	26.71
SCD_{BL}	340	415	350–600	29.75
NCD_{BL}	420	520	420–610	34.26

Bandgap assessment

	HOMO (eV)	LUMO (eV)	λ_{edge} (nm)	E_g^{opt} (eV)
CD_{BL}	−5.22	−1.57	340	3.65
SCD_{BL}	−3.74	−0.30	360	3.44
NCD_{BL}	−3.80	−0.85	420	2.95

Fig. 2(b). When the pH was between 9 and 12, the fluorescence intensity was generally consistent, but it dropped when the pH was very low. Conversely, the fluorescence spectra show that the NCD_{BL} fluorescence intensity progressively drops as the pH gradually drops from 12 to 2.[55,57] Furthermore, it is now becoming clear that the pH of the solution impacts the fluorescence stability of CDs. Under the light of a 365 nm UV lamp, the fluorescence of the NCD_{BL} solution shifts from blue to green shades. Fluorescence intensity is highest at pH 9–12. However, under strongly acidic conditions, the fluorescence eventually decreases. So, based on these emission results and the visual appearance of blue to green shades, it can be concluded that NCD_{BL} has the potential to be explored as a pH sensor. The primary objective of this study was to evaluate the effectiveness of the prepared sensor for monitoring food freshness, where pH levels typically shift toward the acidic side. However, since the CD_{BL} (pH 6) and SCD_{BL} (pH 2) were already acidic by nature, their response to further decreases in pH was not significant. Due to this limitation, they were not considered ideal for sensing in acidic environments. These materials might instead be more effective for applications where pH changes toward the basic side are more relevant.

The bandgap energies of CDs were calculated using eqn (1):

$$E_g^{opt} = \frac{1240}{\lambda_{edge}} \quad (1)$$

where λ_{edge} represents the wavelength corresponding to the highest absorption edge and E_g^{opt} is the bandgap.[55] The determined bandgap energies exhibit a progressive decline from 3.65 eV to 2.95 eV with increasing particle size of the CDs, as indicated in Table S3.† Using eqn (2) and Tauc plots (Fig. S5†), the bandgap values have been elucidated as well.[58] Similar trends resulted in decreased bandgap from CD_{BL} to NCD_{BL} (bandgap values using Tauc plots were found to be 4.11 eV, 4.03 eV, and 3.79 eV for CD_{BL}, SCD_{BL}, and NCD_{BL}, respectively):

$$\alpha h\nu^n = \alpha_0 h\nu - \alpha_0 E_g^{opt} \quad (2)$$

where α is the absorption coefficient, $h\nu$ is the photon energy, α_0 is the proportionality factor, E_g^{opt} is the optical bandgap and n is the exponent that describes transitions (n = 2 for indirect ones and $n = \frac{1}{2}$ for direct ones). This finding confirms the presence of the quantum size effect in CDs. The HOMO energy levels were obtained using UV photoelectron spectroscopy, whereas the LUMO energy levels were computed based on the optical bandgap energy and the HOMO energy levels (Table 1).[55] The energy diagram depicted in Fig. 2(c) demonstrates the declining patterns of HOMO and LUMO levels (the disparity between the bandgap and HOMO levels). These results clearly explain the interband transitions in the CDs upon doping.

2.5. Applicability of the prepared CD_{BL} and CNC_{BL} hybrids

This part of the study extensively examined the material's capacity to prevent counterfeiting, which is crucial for food authenticity. Tested antimicrobials avoided bacterial growth, extending food shelf-life and safety. Monitoring food conditions in real time adds security and quality control. Finally, the material decomposes efficiently, reducing its environmental impact. Our food packaging is a pioneering material in terms of safety, quality, and environmental responsibility due to its multifarious qualities.

2.5.1. As an anti-counterfeit ink. The aforementioned results indicate that this material exhibits a highly responsive behavior towards UV light, resulting in a reversible transformation of luminescence when exposed to ordinary light, rendering it invisible. This discovery led us to develop a method for encoding information and preventing counterfeiting by utilizing this material, specifically CNC_{BL} and CD_{BL}, as an invisible security ink. The prepared CNC_{BL} suspension and CD_{BL} were formulated in the form of ink and used on a stencil *via* spray coating, as shown in Fig. 3(a); 1 mL of the formulated ink was sprayed on 230 GSM white paper. Then, it was dried in a hot air oven at 40 °C. Then, the encrypted paper was exposed to the 365 nm UV irradiation. The CNCs did not give any response to the UV light, whereas the CD_{BL}-doped CNCs showed excellent results on the paper. On one side, they are invisible in normal light, whereas on the other side, they are visible under UV stimuli.

Such inks are essential for food safety as they authenticate and verify food products, ensuring that consumers receive genuine items free from harmful substances. UV-visible marks and holograms make these inks hard to copy, preventing counterfeiting. They can carry scannable information to track the product's origin and supply chain, addressing safety issues quickly. Anti-counterfeit measures increase consumer trust in product authenticity and safety and assist producers in meeting regulatory requirements. Nanotechnology-based inks improve security, protecting legitimate manufacturers from counterfeits and brand damage. Anti-counterfeit inks safeguard public health and food safety by guaranteeing only authenticated items to customers.

2.5.2. As an antimicrobial film. This application involves the study of the responses of prepared materials when exposed to the bacteria *S. aureus* (SA) and *P. aeruginosa* (PA). SA is known to infect food items, ranking in the top five foodborne

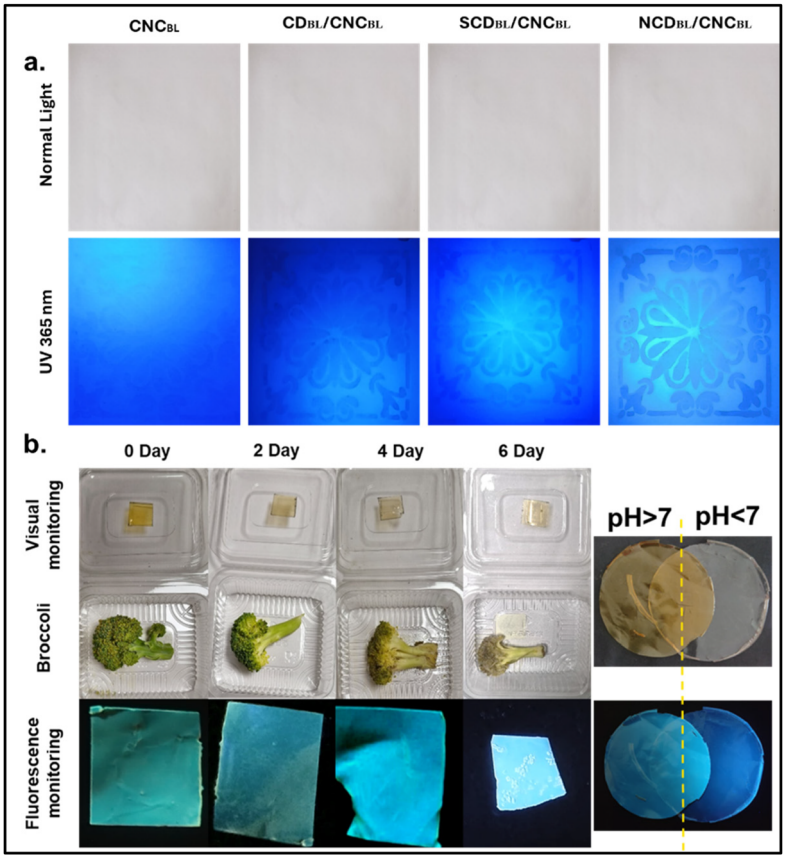

Fig. 3 (a) Anti-counterfeit potential of the prepared inks *via* using the spray coating method, and (b) freshness monitoring of broccoli using prepared NCD_{BL}/CNC_{BL}-based sensors under visual and UV irradiation stimuli.

pathogens. In contrast, PA is also frequently reported in drinking water and food items, causing spoilage and spreading diseases.[59,60] The antimicrobial activity of CD_{BL}, SCD_{BL}, and NCD_{BL} was compared by selecting two strains of bacteria, PA (Gram-negative) and SA (Gram-positive), in the concentration range of 0.5 mg mL^{-1} to 15 mg mL^{-1}. The minimum inhibitory concentration (MIC) is the observed minimum amount of drug or nanoparticles that can resist or inhibit the propagation of bacterial cells (Fig. 4(a) and Table S3†). The CD_{BL} showed no bacterial growth inhibition or bacterial killing towards both the strains of PA and SA. Meanwhile, the MIC for SCD_{BL} is discerned to be 6 mg mL^{-1} for both PA and SA, whereas the MIC for NCD_{BL} was found to be 1.5 mg mL^{-1} towards PA and 2.5 mg mL^{-1} for SA. NCD_{BL} shows ameliorated antimicrobial activity compared to CD_{BL} and SCD_{BL}, with MKC values of 2.5 mg mL^{-1} and 6 mg mL^{-1} for PA and SA, respectively. Meanwhile, SCD_{BL} shows MKC around 10 mg mL^{-1} for bacteria. The FESEM images of film incorporated with CNC_{BL}, CD_{BL}/CNC_{BL}, SCD_{BL}/CNC_{BL}, and NCD_{BL}/CNC_{BL} were analyzed for bacterial growth and killing. In the case of CNC_{BL}, CD_{BL}/CNC_{BL}, and SCD_{BL}/CNC_{BL}, the films did not exhibit microbial killing as MKC was at a higher dose for SCD_{BL}, whereas CD_{BL} lacked antimicrobial activity. However, SCD_{BL}/CNC_{BL} and NCD_{BL}/CNC_{BL} showed lesser microbial load than CNC_{BL}/CNC_{BL} and CD_{BL}/CNC_{BL} (Fig. 4(b)). This gives an inference that these films have inhibited bacterial growth. In the NCD_{BL}/CNC_{BL} films, a small amount of fused bacterial cells was observed, confirming that these films had a slight potential to kill the loaded bacterial cells. NCD_{BL} and NCD_{BL}/CNC_{BL} have shown better results during the antimicrobial testing than undoped and sulfur-doped CDs (Fig. 4(c)). This may result from the generation of enhanced reactive oxygen species in the presence of nitrogen, as observed by Niu *et al.* and Madrid *et al.* in their research.[61,62]

The prepared films were also investigated for thermal and mechanical stability (Fig. S6†). The prepared films showed first weight loss at 125 °C due to the loss of unbound moisture, and the second loss was observed in the range of 200–370 °C, which may be due to the breakage of carbon bonds in the films, while the third degradation was observed in the rage of 410–550 °C; at this stage, char formation occurred. The mechanical strength of the CD-doped films was greater than that of the neat CNC_{BL} films, which raises the idea that the CDs, apart from the optical microbial pH response, also give rise to the reinforcement of the CNC_{BL} films.

Such films suppress food-spoiling bacteria, extending shelf-life and minimizing the risk of foodborne diseases caused by pathogens. These films reduce the need for chemical preserva-

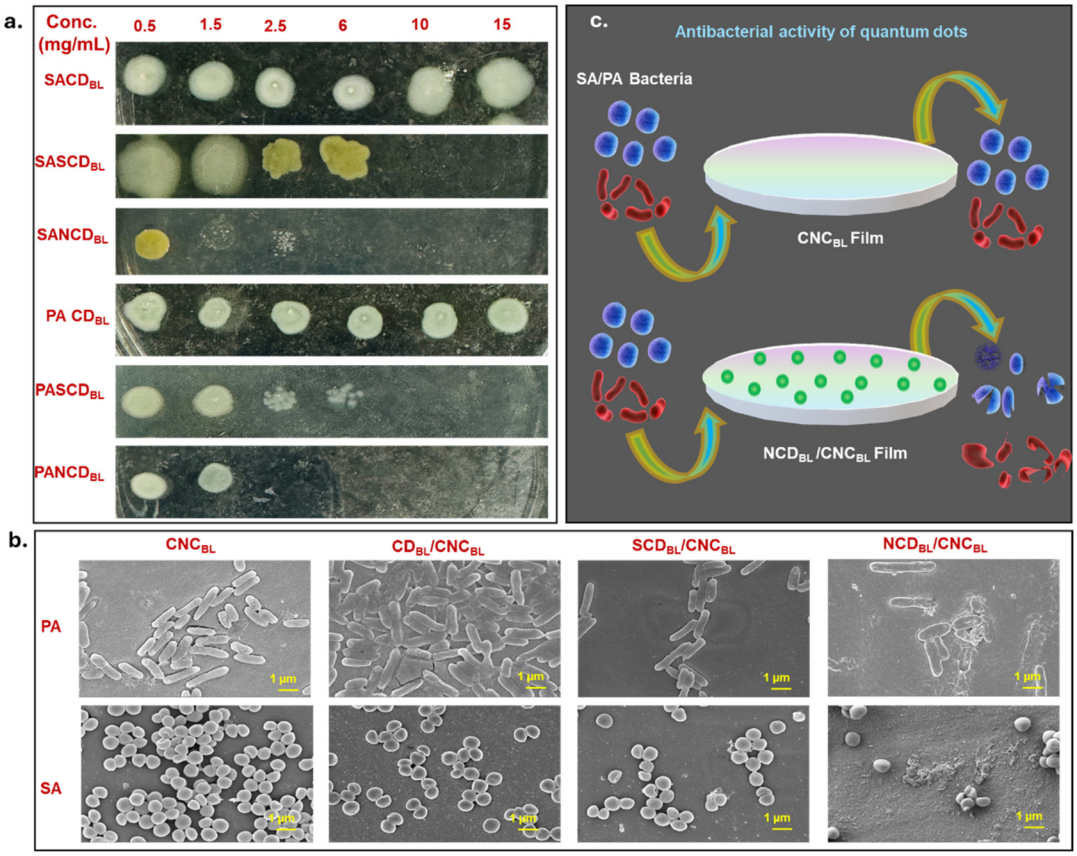

Fig. 4 Antimicrobial properties of the prepared CDs and sensors. (a) Minimum inhibitory concentration (MIC) calculations, (b) potential assessment of the prepared films against bacterial growth and their killing, and (c) antibacterial activity of the prepared NCD_{BL}/CNC_{BL} films.

tives, matching customer expectations for natural products, and keep food fresh and tasty by maintaining sensory and nutritional quality. Food safety across the supply chain is vital for worldwide distribution networks, and environmental benefits from biodegradable materials are improved. They avoid spoiling, saving producers, merchants, and consumers money. Antimicrobial films improve food packaging technology, improving health, sustainability, and efficiency.

2.5.3. As a sensor in packaging and its biodegradability. Carbon dots (CDs) are regarded as highly biocompatible nanoparticles with low toxicity. For instance, graphene quantum dots, which share a similar structure with the CDs being studied herein, have shown low or no toxicity to living organisms, regardless of surface modification, even when administered in a single dose.[63] This allowed us to use such materials in food freshness sensing. In this study, we chose to monitor the freshness of broccoli. Broccoli contains essential vitamins and minerals, including vitamin C, calcium, and iron. Broccoli is considered an exotic vegetable and is generally unavailable in local markets. As broccoli ages, enzymatic and metabolic processes modify its pH. Hence, monitoring the pH level is essential for studying the storage of broccoli. A modestly high pH in fresh broccoli is typical, but as pH decreases, suggesting the breakdown of organic compounds and accumulation of acidic substances, it signals microbial activity and deterioration.[64,65] This information helps determine broccoli quality during storage and transportation, affecting consumer satisfaction through texture, flavor, odor, and nutrient content. Monitoring pH also detects microbial growth, leading to prompt interventions to maintain freshness and reduce pathogen health hazards.[66,67] Real-time pH monitoring in contemporary packaging technology helps maintain food quality and safety.[68] Thus, pH monitoring helps broccoli reach customers in good condition, supporting quality assurance and public health goals.

We prepared CNC_{BL}, CD_{BL}/CNC_{BL}, SCD_{BL}/CNC_{BL}, and NCD_{BL}/CNC_{BL} sensing films to monitor food freshness. Due to the responsiveness of NCD_{BL} and its film with CNC_{BL} towards pH and microbial growth inhibition and killing, we selectively focused on NCD_{BL}/CNC_{BL} for the quality monitoring of broccoli freshness. The prepared sensor demonstrated a sensing ability to sense the freshness of the broccoli. Incremental visual and fluorescence color changes in the sensor were observed over a number of days (Fig. 3(b)). As broccoli's pH changes towards the acidic side, the color of the sensor changes from greenish to greenish with a blue tinge. Visually, the color changes from brown to light brown. To confirm that the color change is due to a change in pH, we exposed the film

to acid fumes and observed similar optical changes. The pH of broccoli decreases, as observed *via* pH analysis after grinding the broccoli and mixing it in 80 mL of DI water (as summarized in Table S3†). Apart from this, the solid content of broccoli decreased with time due to its degradation; the solid content was detected at its maximum in the case of the NCD_{BL}/CNC_{BL} sensor (as summarized in Table S3†). In comparison with other fabricated sensors, Zhu *et al.*designed one with cellulose nanofibers (CNFs) and CDs for food freshness monitoring.[69] Similarly, Si *et al.* proposed lignin-derived CDs for food freshness monitoring, but they did not establish the antimicrobial potential of their material,[70] which is a limitation toward its use for food packaging. This gives an edge to our work in that these sensors also inhibit bacterial growth, which results in food degradation in broccoli, as confirmed in the antimicrobial tests.

These sensors can be pivotal in ensuring food safety by real-time monitoring of parameters like pH within food packaging. They improve storage conditions and minimize supply chain deterioration and contamination. Packaging sensors made of biodegradable materials promote sustainable packaging by reducing its environmental impact and carbon footprint. These dual functions of monitoring food safety and supporting environmental sustainability through biodegradability show the importance of packaging sensors in modern food packaging systems and contribute to the sustainable development goals set by the United Nations.

The biodegradability of the manufactured sensors was evaluated by burying them in soil alongside periodic visual inspections. Fig. 5(a) shows photographs illustrating the course of degradation. Considering that the main component of the films was cellulose, a material that can be degraded naturally, it was expected that the films would degrade quickly. During the initial 48 hours, the film surfaces developed creases, most likely due to absorbing moisture from the surrounding environment. Thorough examinations indicated that after 29 days, the films had undergone degradation of 98–99%, leaving no discernible remnants on the grid (as summarized in Table S4†).

Nevertheless, films that included CD_{BL}/CNC_{BL}, SCD_{BL}/CNC_{BL}, and NCD_{BL}/CNC_{BL} exhibited considerable amounts of cellulose and experienced up to 98.16% degradation. The variation in degradation rates can be ascribed to loaded CD_{BL}, SCD_{BL}, and NCD_{BL}, which provide supplementary stability to the sensors, hence decelerating their degradation. Although the biodegradability investigation results show that natural processes can break down the CNC_{BL}, CD_{BL}/CNC_{BL}, SCD_{BL}/CNC_{BL}, and NCD_{BL}/CNC_{BL} composite sensors, the rate at which they degrade is lowered as the amount of CD_{BL}, SCD_{BL}, and NCD_{BL} in the sensors is increased.

In order to ascertain whether the sensor that was manufactured had migrated into the soil or had undergone degradation, an examination using Fourier transform infrared (FTIR) spectroscopy was conducted on soil samples both before and after degradation. The results of this study are depicted in Fig. 5(b). After degradation, the Fourier transform infrared (FTIR) spectra of the soil exhibited multiple new peaks that were not present in the spectra of the soil before degradation. An observable peak at around 870 cm^{-1} was detected, indicating the creation of acetal due to the reduction of cellulose aldehyde groups.[71,72] Furthermore, a wide signal centered at 2150 cm^{-1} was detected, suggesting the creation of

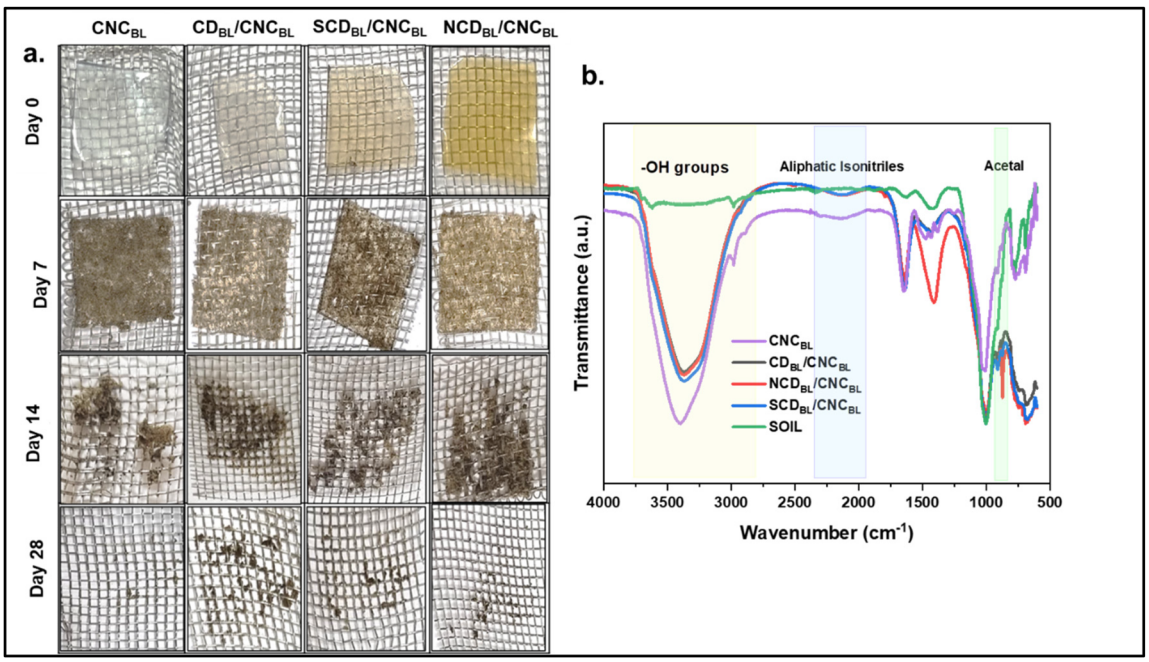

Fig. 5 (a) Biodegradability of the prepared sensor films, and (b) FTIR analysis of soil after sensor film degradation to confirm biodegradation.

aliphatic isonitriles on the cellulose aldehyde groups in the presence of amine moieties found in the soil.[73,74] In addition, a broad peak ranging from 2825 to 3780 cm^{-1} was detected, indicating the presence of –OH groups in cellulose.[34] The existence of these peaks affirms that the sensor component underwent degradation instead of migrating into the soil.

2.5.4. Application prospects of prepared inks and films in terms of their cost and comprehensive performance. Previous sections have explored the practical use of CDs/CNC_{BL}-based inks and films, which show great potential for applications in detecting food freshness and preventing counterfeiting. This is because they possess outstanding performance qualities. Their high sensitivity and biodegradability make them well-suited for use in food packaging. Additionally, their distinct optical features and possibilities for customization make them effective in preventing counterfeiting. The utilization of such technology is typically restricted due to manufacturing and cost constraints. To clarify, we conducted a cost study (summarized in section S3†) of the generated material and determined that it is highly cost-effective, as indicated in Tables S5 and S6.† The cost evaluation of the synthesized composites has been performed at the laboratory level, and expenses may fluctuate when transitioned to industrial production due to supplementary costs such as transportation and catalytic agents. The technology employed in this study is efficient, utilizing CNCs, and the creation of CDs is uncomplicated, necessitating just minimal quantities. The economical and readily scalable manufacturing process for these materials guarantees widespread adoption without financial strain, rendering them an attractive choice for organizations aiming to improve food safety and product security.

3. Conclusions

This study effectively demonstrated the extraction of cellulose nanocrystals (CNC_{BL}) and the production of carbon dots (CDs) from waste black lentil (BL) shells, providing a sustainable and high-performance alternative to conventional sources. The elevated carbon content in BL resulted in a better quantum yield (QY) relative to other bio-based sources. Nitrogen (NCD_{BL}) and sulfur (SCD_{BL}) doping, accomplished *via* ethylene diamine and ammonium persulfate, respectively, was validated through X-ray photoelectron spectroscopy (XPS) and Fourier transform infrared (FTIR) analysis. The CDs, with diameters from 3 to 6 nm as ascertained by HRTEM, had energy bandgaps between 3.65 and 2.95 eV, which decreased with larger particle size. Incorporating CNC_{BL} and CDs into multipurpose films resulted in the creation of a versatile system with applications in anticounterfeiting and real-time food freshness monitoring. The UV-visible ink formed from these components was imperceptible under standard illumination but became distinctly visible under UV light at 365 nm. Furthermore, the films exhibited significant antibacterial activities, with minimum inhibitory concentration (MIC) and minimum killing concentration (MKC) values of 1.5 mg mL^{-1} and 2.5 mg mL^{-1}, respectively. They exhibited a pH-responsive color change, facilitating effective detection of food contamination. The films completely biodegraded within 29 days in soil, highlighting their environmental compatibility. The suggested technology integrates anticounterfeiting features, food freshness detection, antibacterial properties, and biodegradability into a single material, providing a comprehensive and multifunctional solution for food packaging. The fabrication of this economical and readily produced substance represents a substantial improvement over current technologies, offering a novel solution to food safety and authenticity issues.

4. Materials and methods

4.1 Materials

Ethanol (C_2H_5OH 99.9% purity) was purchased from Changshu Hongsheng Fine Chemical Co. Ltd. Toluene (C_7H_8), ammonium persulfate, ethylene diamine, sodium chlorite ($NaClO_2$), sodium sulfite (Na_2SO_3), glacial acetic acid (CH_3COOH), potassium hydroxide (KOH), dimethylsulfoxide {$(CH_3)_2SO$}, sulfuric acid (H_2SO_4), sorbitol and dialysis membrane-110 with a capacity of 3.63 mL cm^{-1} were purchased from HiMedia Pvt. Ltd, India while the double distilled water used in this work was procured from the laboratory distillation unit. Chemicals of analytical grade were employed for this research.

4.2 Proximate and ultimate analysis of *Vigna mungo* waste

Chemical and structural analyses were conducted on the unprocessed material to determine its purity and chemical composition. For compositional analysis, the wood from *Vigna mungo* was rinsed, sun-dried, and pulverized into a homogeneous form. The study strictly adhered to the guidelines set forth by the Technical Institute of the Pulp and Paper Industry (TAPPI). In order to quantify moisture, ash, alpha-cellulose, holocellulose, acid-insoluble lignin (Klason lignin), and solvent extractives, the experimental conditions were evaluated. The additional information (section S1†) contains a detailed explanation of the proximate analysis. The final analysis used the CHNS Elementar Analysensysteme (Vario Micro Cube, Waltham, MA, USA) with helium as the carrier gas and temperatures ranging from 950 to 1200 °C for 0.1 to 6 minutes of combustion duration.

4.3 Fabrication of CD/CNC inks and films to be used as anticounterfeit, antibacterial, and food packaging sensors

Before the fabrication of the inks and films, the cellulose nanocrystals were isolated from untreated *Vigna mungo* waste using a method that we have previously documented and briefly mentioned in section S2.1.†[34] Furthermore, the carbon dots were prepared *via* altering the commonly used hydrothermal method. The detailed procedure has been described in section S2.2.†

A 1.5 wt% CNC suspension was prepared in DI as a stock solution for antimicrobial tests. A 2.5 wt% solution of CD_{BL},

NCD_{BL}, and SCD_{BL} was prepared in DI. Three different CNC_{BL} solutions were prepared by mixing 30 mL of 1.5 wt% CNC suspension with 1 mL of 2.5 wt% of CD_{BL}, SCD_{BL}, and NCD_{BL}. The prepared suspension was cast on a Petri plate with a 10 cm diameter.

The food sensor was prepared by mixing 30 mL of stock solution with 450 microliters of sorbitol (1.5 wt%) for each case of neat CNC_{BL}, CD_{BL}, SCD_{BL}, and NCD_{BL} films to avoid brittleness and the films were similarly cast for antimicrobial testing.

4.4 The quantum yield of prepared CDs

Rhodamine 6G, which has a known quantum yield of 0.95, was employed as a reference to determine the quantum yield of carbon dots (CDs). The CDs and rhodamine 6G solutions were prepared with UV-visible absorption peaks that were maintained at or below 0.1. The absorption and fluorescence spectra were recorded at optimized excitation wavelengths of 360, 340, and 420 nm for CD_{BL}, SCD_{BL}, and NCD_{BL}, respectively. The fluorescence peak areas were measured using fluorescence spectra. The quantum yield was determined by employing eqn (3):

$$QY = QYs \times \frac{I}{I_s} \times \frac{A_s}{A} \times \frac{\eta^2}{{\eta_s}^2} \times 100\% \quad (3)$$

QY is the quantum yield of the CDs. QYs is the quantum yield of the reference, which is rhodamine 6G. I and I_s are the integral areas of the fluorescence peaks for the CDs and the reference, respectively. A and A_s are the absorbance values of CDs and the reference, respectively. The terms η and η_s are the refractive indices of the respective solvents.

4.5 Antimicrobial

4.5.1 *In vitro* assessment of MICs and MKCs. The Gram-positive (*S. aureus*) and Gram-negative (*P. aeruginosa*) bacterial strains were revived from long-term freezing and selected for the antimicrobial study. The broth microdilution method was availed to render the minimum inhibitory concentration (MIC) and minimum killing concentration (MKC) of CD_{BL}, SCD_{BL}, and NCD_{BL} following CLSI guidelines 33. The pure bacterial cell culture was propagated in Luria Bertani (LB) media overnight at 200 rpm at 37 °C. The suspensions of bacterial cultures were then maintained using Mueller–Hinton (MH) media. A sterile 96-well polypropylene plate was deployed for broth dilution assay, having ~109 CFU mL^{-1} bacterial cells per well concurrently; wells were treated with two-fold serial dilution of CD_{BL}, SCD_{BL}, and NCD_{BL} in concentrations ranging from 0.5 mg mL^{-1} to 15 mg mL^{-1}, while taking the negative control of culture media without bacterial cells. The OD values of plates after incubation were measured at 600 nm using a plate reader (BR-580, BR BIOCHEM), where bacterial culture wells with no propagation at the lowest concentration of nanoparticles were considered for the MIC determination. Concurrently, MKCs for the nanoparticles were evaluated by taking 5 μL of bacterial cells with no growth and spotting this volume on MHB agar plates. The plates were kept at 37 °Cover 24 h for the incubation. The minimum number of nanoparticles at which no growth of bacterial colonies was observed was established as the MKC. The determination of the MIC and MKC was performed in triplicate.

4.5.2 Measurement of antimicrobial and adherence properties. The bacterial growth and adherence properties of prepared films with CNC, CD, SCD and NCD incorporated were determined by taking PA and SA log phase cell suspension in LB media and incubating at 37 °C for 12 h at 200 rpm. The CNC, CD, SCD, and NCD films were cut into pieces of surface area 2 cm^2 and kept in 6-well plates; meanwhile, bacterial cells were diluted to maintain up to ~109 CFU mL^{-1} in each well. The 6-well plate was incubated for 24 h at 37 °C, followed by the removal of bacterial planktonic cells containing media and washing films with phosphate buffered saline (PBS) three times to remove unattached cells. The film containing bacterial cells was fixed with 2.5% glutaraldehyde and dried overnight at RT. Further films were dried with ethanol gradients of 20%, 40%, 50%, 70%, 80%, and 100%, followed by air-drying to remove any moisture retained in the samples. The samples were sputter coated with ultrathin gold for the FESEM (Gemini Zeiss)-based morphological analysis of the bacteria upon the films.

4.6 Broccoli freshness monitoring

The broccoli was packed in transparent boxes with CD_{BL}/CNC_{BL}, NCD_{BL}/CNC_{BL}, and SCD_{BL}/CNC_{BL} film tags to measure its pH and check its quality (solid content) for one week. For the weekly study, we ground broccoli samples taken from each of the CD_{BL}/CNC_{BL}, NCD_{BL}/CNC_{BL}, and SCD_{BL}/CNC_{BL} film-tagged boxes, grinding them properly and checking their solid content percentages. Furthermore, this ground broccoli was mixed properly in 80 mL of water, and its pH was checked with a pH meter. This process was done over 2 days, 4 days, 6 days, and 8 days. Based on our observations, Table S4† shows percentage solid content and pH changes of the broccoli. It was observed that the solid content of broccoli decreased from the first day to day 8; its pH also changed, and shifting to an acidic medium.

4.7 Biodegradability test

Biodegradability testing of the manufactured CDs/CNC_{BL} films was conducted using the method described. The experiment was carried out in a plastic container filled with decomposed soil that had been gathered from a pristine and fruitful location on the campus of IIT Roorkee Saharanpur. Before evaluation, the specimens were sectioned into 2 × 2 cm^2 pieces and desiccated in an oven for at least 24 hours to eliminate moisture. The specimens that had been cut were subsequently positioned on a lattice and submerged in the soil to a distance of 40 mm from the partitioned surface of the polypropylene container. The sample-containing PP container was subsequently maintained at 25 ± 3 °C. Additionally, daily water sprinkling was used to stabilize the soil's humidity. Images were acquired until the surface area changes of the film were

visually observed in the samples, and traces were reduced to a minimum on the mesh. The weight loss percentage was computed and subsequently communicated into the research.

5. Characterization techniques

5.1 Structural analysis

ATR mode of the structural analysis of cellulose subsequent to the chemical purification of wood was performed by using a Fourier transform infrared (FTIR) spectrometer manufactured by PerkinElmer. The spectrometer was operated in transmission mode, covering a range of 4000–400 cm^{-1}, with a resolution of 4 cm^{-1} and running 32 scans. The XPS analysis was conducted with a PHI-5000 Versa Probe III X-ray photoelectron spectrometer manufactured by ULVAC-PHI Inc. The spectra were recorded while using analyzer pass energies of 55 eV for individual element spectra and 280 eV for the survey scans, with an Al Kα radiation source. X-ray diffraction (XRD) was conducted at room temperature using a Rigaku Ultima IV (Japan) equipped with an X-ray tube of 40 kV and 40 mA rating, emitting Cu Kα radiation with a wavelength value of 1.54 Å. The diffraction patterns were acquired by scanning at a rate of 4° min^{-1} across a goniometer angle (2θ) ranging from 5 to 45°.

5.2 Morphological analysis

The specimens obtained were examined using a Carl-Zeiss-Gemini field emission scanning electron microscope (FE-SEM) to evaluate their morphology. Before conducting image scanning, a thin layer of Au–Pd was applied to each sample to impart conductivity. A JEM 3200FS electron microscope was used to examine the bulk morphology and particle size distribution.

5.3 Optical analysis

The fluorescence (photoluminescence) of the prepared samples was observed using a Cary Eclipse fluorescence spectrophotometer manufactured by Agilent Technologies (made in Malaysia), and spectra were plotted to check for the emission activity. A Shimadzu (UV-2600) UV-visible spectrophotometer was employed for the UV-visible absorption spectra using a scanning spectrophotometer. UPS analysis was conducted with a PHI-5000 Versa Probe III ultraviolet photoelectron spectrometer manufactured by ULVAC-PHI Inc.

5.4 Thermal and mechanical analysis

A thermogravimetric analyzer instrument (TGA 55, TA, USA) was used for thermogravimetric analysis (TGA). The investigation was performed within the 30–700 °C temperature range, utilizing a nitrogen atmosphere and a heating rate of 5 °C min^{-1}. The tensile strength (TS) of the fabricated CDs/CNC_{BL} films was examined using a universal testing machine (UTM, Instron, NJ, USA). The films were cut into 90 mm long by 10 mm wide pieces and clamped vertically. The strain rate was set at 5 mm min^{-1}, and the breaking force value was recorded. The experiment was completed according to the standard ASTM D 638.

Author contributions

S.S.: conceptualization, methodology, formal analysis, validation, investigation, and writing. K.D.: investigation, validation, and formal analysis. S.B.: methodology, formal analysis, and validation. D.R.: formal analysis and validation. K.R. S: formal analysis and validation. K.M.P.: formal analysis and validation. K.G.: supervision and writing – editing. P.K.M.: conceptualization, methodology, supervision, and writing – editing.

Data availability

The authors confirm that the data supporting the findings of this study are available within the article and in its ESI,† and it will be shared on request.

Conflicts of interest

The authors affirm that they have no discernible financial or interpersonal conflicts that could have potentially impacted the research findings presented in this study.

Acknowledgements

This research has received support from the National Buildings Construction Corporation Ltd, under the project Grant No. NBC-2293-PPE. Shiva Singh and Shakshi Bhardwaj would like to express their sincere appreciation to the Prime Minister's Research Fellowship Programme, financed by the Government of India, for the financial assistance provided.

References

1 V. Maritano, P. Barge, A. Biglia, L. Comba, D. Ricauda Aimonino, C. Tortia and P. Gay, *J. Food Prot.*, 2024, **87**, 100251.
2 K. Muthamma, D. Sunil and P. Shetty, *Appl. Mater. Today*, 2021, **23**, 101050.
3 Y. Shen, X. Le, Y. Wu and T. Chen, *Chem. Soc. Rev.*, 2024, **53**, 606–623.
4 B. Wang and S. Lu, *Matter*, 2022, **5**, 110–149.
5 A. Abdollahi, H. Roghani-Mamaqani, B. Razavi and M. Salami-Kalajahi, *ACS Nano*, 2020, **14**, 14417–14492.
6 X. Yu, H. Zhang and J. Yu, *Aggregate*, 2021, **2**, 20–34.
7 R. Simões, J. Rodrigues, V. Neto, T. Monteiro and G. Gonçalves, *Small*, 2024, **20**, 2311526.
8 K. Jiang, L. Zhang, J. Lu, C. Xu, C. Cai and H. Lin, *Angew. Chem., Int. Ed.*, 2016, **55**, 7231–7235.

9 X. Luo, Y. Han, X. Chen, W. Tang, T. Yue and Z. Li, *Trends Food Sci. Technol.*, 2020, **95**, 149–161.
10 P. Ananthi, K. Hemkumar, S. Subasini and A. Pius, *Mater. Today Sustain.*, 2023, **24**, 100609.
11 S. A. Althawab, T. Alsulami, H. Alzahrani and A. Alzahrani, *Colloids Surf., A*, 2024, **698**, 134554.
12 M. Li, P. Zhang, J. Mao, J. Li, Y. Zhang, B. Xu, J. Zhou, Q. Cao and H. Xiao, *J. Environ. Manage.*, 2024, **359**, 121076.
13 B. K. Barman, Ø. Sele Handegård, A. Hashimoto and T. Nagao, *ACS Sustainable Chem. Eng.*, 2021, **9**, 9879–9890.
14 W. Li, H. Zhang, Y. Zheng, S. Chen, Y. Liu, J. Zhuang, W. R. Liu and B. Lei, *Nanoscale*, 2017, **9**, 12976–12983.
15 Y. Chen, G. Xiong, L. Zhu, J. Huang, X. Chen, Y. Chen and M. Cao, *ACS Omega*, 2022, **7**, 6834–6842.
16 J. Liu, R. Li and B. Yang, *ACS Cent. Sci.*, 2020, **6**, 2179–2195.
17 J. Ahn, S. Pak and H. Kim, *Cellulose*, 2021, **28**, 11261–11274.
18 S. Quraishi, S. Plappert, B. Ungerer, P. Taupe, W. Gindl-Altmutter and F. Liebner, *Appl. Sci.*, 2019, **9**, 107.
19 J. Guo, D. Liu, I. Filpponen, L. S. Johansson, J. M. Malho, S. Quraishi, F. Liebner, H. A. Santos and O. J. Rojas, *Biomacromolecules*, 2017, **18**, 2045–2055.
20 S. Singh, S. Bhardwaj, P. Tiwari, K. Dev, K. Ghosh and P. K. Maji, *Mater. Adv.*, 2024, **5**, 2622–2654.
21 S. Singh, S. Bhardwaj, N. Choudhary, R. Patgiri, Y. Teramoto and P. K. Maji, *ACS Appl. Mater. Interfaces*, 2024, **16**, 41743–41765.
22 J. Guo, H. Li, L. Ling, G. Li, R. Cheng, X. Lu, A. Q. Xie, Q. Li, C. F. Wang and S. Chen, *ACS Sustainable Chem. Eng.*, 2020, **8**, 1566–1572.
23 M. Li, W. Yao, J. Liu, Q. Tian, L. Liu, J. Ding, Q. Xue, Q. Lu and W. Wu, *J. Mater. Chem. C*, 2017, **5**, 6512–6520.
24 Y. Liu, L. Zhou, Y. Li, R. Deng and H. Zhang, *Nanoscale*, 2017, **9**, 491–496.
25 B. Fu, Q. Liu, M. Liu, X. Chen, H. Lin, Z. Zheng, J. Zhu, C. Dai, X. Dong and D. P. Yang, *Chin. Chem. Lett.*, 2022, **33**, 4577–4582.
26 Z. Riahi, J. W. Rhim, R. Bagheri, G. Pircheraghi and E. Lotfali, *Prog. Org. Coat.*, 2022, **166**, 106794.
27 S. Roy, H. J. Kim and J. W. Rhim, *ACS Appl. Polym. Mater.*, 2021, **3**, 1060–1069.
28 X. Zhou, M. P. Taylor, H. Salouros and S. Prasad, *Sci. Rep.*, 2018, **8**, 1–11.
29 M. Dwiyaniti, A. G. Elang Barruna, R. Muhamad Naufal, I. Subiyanto, R. Setiabudy and C. Hudaya, *IOP Conf. Ser.: Mater. Sci. Eng.*, 2020, **909**, 012018.
30 I. Okman, S. Karagöz, T. Tay and M. Erdem, *Appl. Surf. Sci.*, 2014, **293**, 138–142.
31 S. Bhardwaj, S. Singh, R. S. Meda, S. Jain and P. K. Maji, *Biomass Convers. Biorefin.*, 2023, DOI: **10.1007/s13399-023-03970-y**.
32 N. Choudhary, S. Singh, G. Malik, S. Bhardwaj, S. Sharma, A. Tomar, S. Issar, R. Chandra and P. K. Maji, *Sustainable Energy Fuels*, 2024, **8**, 3595–3609.
33 R. S. Meda, S. Jain, S. Singh, D. Ramakanth, S. Bhardwaj, Y. Teramoto, P. Mondal and P. K. Maji, *ACS Omega*, 2024, **9**, 33386–33396.
34 S. Singh, S. Bhardwaj, C. Verma, M. Chhajed, K. Balayan, K. Ghosh and P. K. Maji, *J. Mol. Liq.*, 2022, **366**, 120326.
35 L. Segal, J. J. Creely, A. E. Martin and C. M. Conrad, *Text. Res. J.*, 2016, **29**, 786–794.
36 F. Khili, J. Borges, P. L. Almeida, R. Boukherroub and A. D. Omrani, *Waste Biomass Valorization*, 2019, **10**, 1913–1927.
37 F. V. Ferreira, M. Mariano, S. C. Rabelo, R. F. Gouveia and L. M. F. Lona, *Appl. Surf. Sci.*, 2018, **436**, 1113–1122.
38 Y. C. G. Kwan, G. M. Ng and C. H. A. Huan, *Thin Solid Films*, 2015, **590**, 40–48.
39 S. Majhi and M. Sikdar (née Bhakta), *3 Biotech*, 2023, **13**, 155.
40 S. Zhu, K. Wang, J. Hu, R. Liu and H. Zhu, *Mater. Adv.*, 2020, **1**, 3176–3181.
41 A. Kumar and C. Sharma, *Anal. Bioanal. Chem.*, 2023, **415**, 3435–3448.
42 A. Kumar and C. Sharma, *J. Mol. Liq.*, 2024, **410**, 125561.
43 C. Xu, Q. Han, Y. Zhao, L. Wang, Y. Li and L. Qu, *J. Mater. Chem. A*, 2015, **3**, 1841–1846.
44 S. Huang, E. Yang, J. Yao, Y. Liu and Q. Xiao, *Anal. Chim. Acta*, 2018, **1035**, 192–202.
45 C. Wang, H. Shi, M. Yang, Z. Yao, B. Zhang, E. Liu, X. Hu, W. Xue and J. Fan, *Colloids Surf., B*, 2021, **205**, 111874.
46 H. R. Chen, W. M. Meng, R. Y. Wang, F. L. Chen, T. Li, D. D. Wang, F. Wang, S. E. Zhu, C. X. Wei, H. D. Lu and W. Yang, *Carbon*, 2022, **190**, 319–328.
47 Z. Kassab, I. Kassem, H. Hannache, R. Bouhfid, A. E. K. Qaiss and M. El Achaby, *Cellulose*, 2020, **27**, 4287–4303.
48 S. Collazo-Bigliardi, R. Ortega-Toro and A. Chiralt Boix, *Carbohydr. Polym.*, 2018, **191**, 205–215.
49 J. De Aguiar, T. J. Bondancia, P. I. C. Claro, L. H. C. Mattoso, C. S. Farinas and J. M. Marconcini, *ACS Sustainable Chem. Eng.*, 2020, **8**, 2287–2299.
50 A. Pal, M. P. Sk and A. Chattopadhyay, *Mater. Adv.*, 2020, **1**, 525–553.
51 A. B. Siddique, A. K. Pramanick, S. Chatterjee and M. Ray, *Sci. Rep.*, 2018, **8**, 1–10.
52 K. J. Mintz, M. Bartoli, M. Rovere, Y. Zhou, S. D. Hettiarachchi, S. Paudyal, J. Chen, J. B. Domena, P. Y. Liyanage, R. Sampson, D. Khadka, R. R. Pandey, S. Huang, C. C. Chusuei, A. Tagliaferro and R. M. Leblanc, *Carbon*, 2021, **173**, 433–447.
53 Y. Liu, C. Zhu, Y. Gao, L. Yang, J. Xu, X. Zhang, C. Lu, Y. Wang and Y. Zhu, *Appl. Surf. Sci.*, 2020, **510**, 145437.
54 K. G. Nguyen, M. Huš, I. A. Baragau, J. Bowen, T. Heil, A. Nicolaev, L. E. Abramiuc, A. Sapelkin, M. T. Sajjad and S. Kellici, *Small*, 2024, **20**, 2310587.
55 R. Sekar, N. Basavegowda, S. Jena, S. Jayakodi, P. Elumalai, A. Chaitanyakumar, P. Somu and K. H. Baek, *Pharmaceutics*, 2022, **14**, 1869.
56 S. Miao, K. Liang, J. Zhu, B. Yang, D. Zhao and B. Kong, *Nano Today*, 2020, **33**, 100879.
57 L. Guo, L. Li, X. Wang, Y. Zhang and F. Cui, *ACS Omega*, 2023, **8**, 37098–37107.

58 Z. Chen and T. F. Jaramillo, *The Use of UV-visible Spectroscopy to Measure the Band Gap of a Semiconductor*, 2017, **https://mmrc.caltech.edu/Cary%20UV-Vis%20Int.Sphere/Literature/Spectroscopy%20Jaramillo.pdf**.
59 S. Hameed, Y. Wang, L. Zhao, L. Xie and Y. Ying, *Mater. Sci. Eng., C*, 2020, **108**, 110338.
60 Z. Xu, J. Xie, T. Soteyome, B. M. Peters, M. E. Shirtliff, J. Liu and J. M. Harro, *Curr. Opin. Food Sci.*, 2019, **26**, 57–64.
61 K. K. Niu, C. Q. Ma, R. Z. Dong, H. Liu, S. S. Yu and L. B. Xing, *Nano Res.*, 2024, **17**, 4825–4833.
62 A. Madrid, G. Martinez, F. Hornos, J. Bonet-Aleta, E. Calvo, A. Lozano and J. L. Hueso, *Catal. Today*, 2023, **422**, 114214.
63 H. Kuznietsova, A. Géloën, N. Dziubenko, A. Zaderko, S. Alekseev, V. Lysenko and V. Skryshevsky, *Discover Nano*, 2023, **18**, 1–17.
64 M. I. Gunawan and S. A. Barringer, *J. Food Process. Preserv.*, 2000, **24**, 253–263.
65 E. M. Gonçalves, J. Pinheiro, C. Alegria, M. Abreu, T. R. S. Brandão and C. L. M. Silva, *J. Agric. Food Chem.*, 2009, **57**, 5370–5375.
66 Alum, E. Akanele, Urom, S. Mgbo Otu Chukwu, Ben and C. Mary Ahudie, *Int. J. Sci. Technol. Res.*, 2016, **5**, 65–78.
67 O. Alegbeleye, O. A. Odeyemi, M. Strateva and D. Stratev, *Appl. Food Res.*, 2022, **2**, 100122.
68 J. Siddiqui, M. Taheri, A. Ul Alam and M. Jamal Deen, *Small*, 2022, **18**, 2101171.
69 H. Zhu, J. Li and J. H. Cheng, *Int. J. Biol. Macromol.*, 2024, **271**, 132642.
70 L. Si, Z. K. Shi, J. Y. Hou, C. X. Miao, Q. Hou, Z. Xu and S. Ai, *ACS Appl. Nano Mater.*, 2022, **5**, 16620–16632.
71 S. Veelaert, D. De Wit, K. F. Gotlieb and R. Verhé, *Carbohydr. Polym.*, 1997, **33**, 153–162.
72 S. F. Plappert, S. Quraishi, N. Pircher, K. S. Mikkonen, S. Veigel, K. M. Klinger, A. Potthast, T. Rosenau and F. W. Liebner, *Biomacromolecules*, 2018, **19**, 2969–2978.
73 M. Goda, Y. Hashimoto, S. Shimizu and M. Kobayashi, *J. Biol. Chem.*, 2001, **276**, 23480–23485.
74 M. P. Bernstein, S. A. Sandford and L. J. Allamandola, *Astrophys. J.*, 1997, **476**, 932–942.